Adaptive multiscale reconstruction of buried objects

Alexandre Baussard†§, Eric L. Miller‡, Dominique Lesselier†

† Département de Recherche en Électromagnétisme - Laboratoire des Signaux et Systèmes (CNRS/SUPELEC/UPS), 3 rue Joliot-Curie, 91192 Gif-sur-Yvette, France.
‡ Center for Subsurface Sensing and Imaging Systems, Northeastern University, 315 Stearns Hall, Boston MA 02115-5000, USA.

Abstract. In this contribution, an adaptive multiscale approach for the localization and characterization of buried objects in a half-space is proposed. The main goal of the approach is to reduce the number of elements to be estimated and so to improve the robustness of the inversion and to increase the quality reconstruction. The proposed inversion scheme is based on an adaptive, coarse-to-fine iterative strategy using spline pyramids. The global procedure consists of sequences of non-linear inversions separated by refinement steps, which overall produces an accurate, low-order representation of the sought object.

§ To whom correspondence should be addressed (baussard@lss.supelec.fr)

1. Introduction

The detection and the characterization of objects buried in a half-space from measurements of the scattered response of a known electromagnetic excitation arise in various applications such as Earth subsurface sensing, humanitarian demining, medical imaging, and nondestructive testing. In this paper, the general problem of the non-linearized reconstruction of two-dimensional subsurface heterogeneities is considered. The goal is to retrieve constitutive parameters of buried objects (geometry, electrical characteristics) from time-harmonic wave field data collected above the half-space. This is a challenging problem, in particular due to the severe ill-posedness which is caused by the availability of aspect-limited data only.

Many algorithms have already been developed to solve this kind of inverse scattering problem, such as those in [3, 5, 8, 9, 14]. Typically, these methods solve a large-scale, non-linear optimization problem by generating values for every pixel covering the test area, including those which might not contain any useful information about the objects. In previous work [1, 2], in order to reduce the number of unknowns to be estimated, an adaptive B-spline scheme was proposed. The test domain was represented by a spline surface parametrized by a knot distribution [4] adaptively determined during the process. In the present contribution, starting from this previous work and inspired also from an earlier solution of an one-dimensional inverse scattering problem for a diffusion coefficient [10], an adaptive multiscale approach based on spline pyramids [13] is proposed. This multiscale representation of the unknown parameters enables a low-order reconstruction for which the distribution of fine-scale detail is determined via an automatic refinement procedure. That is, starting with a coarse-scale set of functions, the sought distribution is iteratively refined by introducing finer-scale functions in 'areas of interest' (say, where objects are emerging from the background); then, the final estimate consists of functions at several scales.

The general idea and resulting scheme of the proposed adaptive multiscale approach may look like those of the adaptive B-spline approach proposed in [2]. However, in this previous work, the object was represented in a B-spline basis in which one set of knots was defined along the x-axis and another along the y-axis. The influence of the locations of these knots was somewhat 'global' in that, e.g., a change in the location of an x-axis knot generally impacted the structure of the object in a vertical region covering the whole y-axis. One result of using B-splines in this manner was the presence of artifacts in images where there were multiple disconnected objects in the field of interest. The newly proposed representation, based on spline pyramids, leads to a more 'local' description by which it is meant that each basis permits to individually 'describe' a part of the image, and enables better reconstructions.

Moreover, the presently proposed adaptive coarse-to-fine procedure imposes smoothness conditions at coarse resolutions, which tends to regularize the inversion problem; there is no need for explicit regularization using, e.g., a Tikhonov-type functional (which would involve to set a proper weighting parameter).

The paper is organized as follows. In section 2 the formulation of the problem is introduced. In section 3 the proposed adaptive multiscale algorithm is described. In section 4, some numerical results obtained using the proposed scheme and a standard one (pixel-based conjugate-gradient inversion scheme) are shown. In section 5 concluding remarks are made.

2. Problem statement

The geometry of the problem studied is depicted in figure 1 where two homogeneous half-spaces (numbered 1 and 2) are separated by a planar interface. Possibly inhomogeneous, penetrable cylindrical obstacles (Ω) with z-axis are fully embedded in half-space 2, inside a prescribed domain $\mathcal{D}$.

All constitutive materials are assumed linear, isotropic and non-magnetic. Their permittivities read as $\varepsilon_m = \varepsilon_0 \varepsilon_{rm}$, $m = 1, 2, \Omega$, at implied circular frequency ω – omitting the time-dependence $\exp(-i\omega t)$ – where ε_0 is the permittivity of half-space 1 (henceforth assumed to be air), and where both ε_{r2} and $\varepsilon_{r\Omega}$ might take frequency-dependent, complex values. The corresponding propagation constants k_m are defined as $k_m^2 = \omega^2 \mu_0 \varepsilon_m$.

Ideal time-harmonic electric current line sources S_l ($l = 1, ..., N_s$), set parallel to the z-axis (Transverse Magnetic – TM – polarized), are equally distributed above the interface at constant height y_s. Similarly ideal sensors are also equally distributed above the interface at constant height y_r (domain Γ) and collect the single z-component of the scattered electrical field e^d at N_r locations.

Starting from the Maxwell equations and using the Green theorem, the forward scattering problem is formulated via the usual domain integral equations:

$$e(\mathbf{r}) = e^{inc}(\mathbf{r}) + \int_{\mathcal{D}} \chi(\mathbf{r}') G_{22}(\mathbf{r}, \mathbf{r}') e(\mathbf{r}') d\mathbf{r}', \quad \mathbf{r} \in \mathcal{D}, \tag{1}$$

$$e^d(\mathbf{r}) = \int_{\mathcal{D}} \chi(\mathbf{r}') G_{12}(\mathbf{r}, \mathbf{r}') e(\mathbf{r}') d\mathbf{r}', \quad \mathbf{r} \in \Gamma, \tag{2}$$

where $\chi(\mathbf{r}) = \varepsilon_{r\Omega}(\mathbf{r}) - \varepsilon_{r2}$ is the contrast function defined in $\mathcal{D}$, and e and e^{inc} are the single z-component of the total field and of the incident field, respectively. $G_{mn}(\mathbf{r}, \mathbf{r}')$ are the Green functions which model the radiation of a Dirac-type source at $\mathbf{r}'$ in the half-space n and the observation of the field at $\mathbf{r}$ in the half-space m.

By discretizing the search domain into a regular mesh (N_x cells along the x-axis and N_y cells along the y-axis) and using a standard pulse-basis point-matching method of moments [7], state equation (1) and observation equation (2) can be written, for each illumination l ($l = 1, ..., N_s$), as matrix equations

$$\mathbf{e}_l = \mathbf{e}_l^{inc} + \mathbf{G}_{22} D(\mathbf{c}) \mathbf{e}_l, \tag{3}$$

$$\mathbf{e}_l^d = \mathbf{G}_{12} D(\mathbf{c}) \mathbf{e}_l, \tag{4}$$

where $\mathbf{e}_l$ is the total field vector and $\mathbf{e}_l^{inc}$ is the incident field vector, both of dimension $N(= N_x \times N_y)$, $\mathbf{e}_l^d$ is the scattered field vector of dimension N_r, and $\mathbf{G}_{22}$ and $\mathbf{G}_{12}$ are

$[N \times N]$ and $[N_r \times N]$ matrices made of properly integrated Green functions [6, 7]. $D(\mathbf{c})$ is a $[N \times N]$ diagonal matrix whose entries are the elements of the N-sized contrast vector $\mathbf{c}$.

These two equations can be expressed as a unique non-linear equation in $\mathbf{c}$:

$$\mathbf{e}_l^d = \mathbf{G}_{12}D(\mathbf{c})[\mathbf{I}_d - \mathbf{G}_{22}D(\mathbf{c})]^{-1}\mathbf{e}_l^{inc}, \tag{5}$$

where $\mathbf{I}_d$ denotes the identity matrix of dimension $[N \times N]$.

3. Adaptive multiscale approach

3.1. An overview of spline pyramids

Splines are piecewise polynomials the pieces of which are smoothly connected together. They can be uniquely characterized in terms of a B-spline expansion as

$$s(x, y) = \sum_{k \in Z} \sum_{l \in Z} a(k, l)\beta^n(x - k)\beta^n(y - l), \tag{6}$$

which involves integral shifts of the central B-spline of degree n denoted as $\beta^n(x)$. The parameters of the model are the B-spline coefficients $a(k, l)$. B-splines are symmetrical, bell-shaped functions constructed from $(n + 1)$-fold convolution of a rectangular pulse $\beta^0(x)$:

$$\beta^n(x) = \underbrace{(\beta^0 * \beta^0 * ... * \beta^0)}_{(n+1)\ times}(x) \qquad \text{with } \beta^0(x) = \begin{cases} 1 & \text{if } -\frac{1}{2} < x < \frac{1}{2}, \\ \frac{1}{2} & \text{if } \mid x \mid = \frac{1}{2}, \\ 0 & \text{otherwise.} \end{cases} \tag{7}$$

Within the area of multiscale signal and image processing, B-splines have proven quite useful because they possess a convenient 'nesting' property. That is, a B-spline may be written as a linear superposition of dilated and translated versions of itself. More formally, one has a two-scale dilation equation of the form [11]

$$\beta(x) = \sum_{k=0}^{N_k-1} \alpha_k \beta(2x - k) \tag{8}$$

thereby making B-splines well suited for the synthesis of multiscale processing methods. α_k are the expansion coefficients. In figure 2.b, an illustration of the two-scale relation for a B-spline of degree 3 (figure 2.a) is exemplified.

Spline pyramids provide a very convenient tool for performing multiscale image processing. In [10] the two-scale relationship was exploited in the development of a one-dimensional nonlinear inversion method in which detail was iteratively added and pruned from an underlying representation of the unknown object. The resulting technique provided for an adaptively determined, parsimonious representation of the object in which fine-scale detail was 'automatically' put in the proper areas. Moreover, iterative algorithms based on a multiscale approach tend to be less likely to get trapped in a local optimum, as shown in an image registration algorithm [12, 13].

3.2. Adaptive multiscale algorithm

The solution of the inverse problem consists of building up a map of the distribution of the constitutive parameters (permittivity and/or conductivity) throughout the search domain, from the scattered field data. In this contribution, an adaptive multiscale scheme based on the previous spline pyramids is proposed, which leads to 'describe' the unknown parameters via spline functions at several scales. The distribution should be as follows: fine-scale functions in the object and its vicinity, and coarse-scale functions elsewhere. The key issue is that this distribution is determined automatically by the algorithm with no *a priori* information about the parameters. The contrast function is defined as

$$\mathbf{c} = \mathbf{Ba}, \tag{9}$$

where $\mathbf{a}$ is the expansion coefficient vector of dimension $N_a << N$ and $\mathbf{B}$ is the $[N \times N_a]$ matrix, the columns of which correspond to tensor products of B-spline functions. As basis functions, the popular cubic B-splines (see figure 2.a) are considered for their useful properties of data fitting and smoothness [13].

From (5) and taking into account (9), the inverse problem is solved by minimizing the cost functional:

$$J(\mathbf{a}) = W_n \sum_{l=1}^{L} \|\mathbf{e}_l^d - \mathbf{G}_{12}D(\mathbf{Ba})(\mathbf{I}_d - \mathbf{G}_{22}D(\mathbf{Ba}))^{-1}\mathbf{e}_l^{inc}\|^2, \tag{10}$$

where W_n is a normalizing coefficient defined as

$$W_n = \frac{1}{\sum_{l=1}^{L} \|\mathbf{e}_l^d\|^2} \tag{11}$$

which is introduce in order to have normalized evolutions of the cost functional values and so make easier the comparison of the convergence for each numerical cases. Moreover, this coefficient do not influence the convergence of the cost function. Minimization of (10) is performed in standard fashion via a conjugate-gradient algorithm [2, 5].

The global algorithm takes advantage of the iterative nature of the minimization procedure by adapting the local resolution of the object between sequences of iterations. This adaptive multiscale algorithm, which is a coarse-to-fine procedure, can be described as follows:

S1 - From a coarse collection of cubic B-splines (e.g., figure 3.b), minimize (10).

S2 - Iterative procedure

    S2.1 - Refine the representation by introducing a finer scale representation in 'areas of interest' (i.e., obstacles emerging in the search domain).

    S2.2 - Minimize (10), using as initial guess the previous object estimation.

    S2.3 - Go back to S2.1 until the representation cannot be refined anymore, until the minimal criterion value is reached, or until the maximum number of iterations is reached (the number of iterations in the minimization steps S1 and S2.2

and the number of iterations of stage S2 can be fixed at the begining of the procedure).

The goal at refinement stage S2.1 is to replace a B-spline by its finer-scale representation only within those areas where it appears interesting to get a more detailed representation, as already indicated. The strategy in S2.1 summarizes as follows: one is replacing a B-spline by its finer representation, and ~~one is~~ subsequently attempting to estimate whether or not this new representation has any positive influence on the image reconstruction, i.e., on the value of the cost functional. Since this approach requires the solution of a non-linear optimization problem, it might unduly increase the computational burden of the global procedure. So, in order to avoid this situation, the total field is kept constant during S2.1. Let us emphasize that this 'linearization' does not influence directly the reconstruction since one just considers here whether or not a more detailed representation of local parts of the image might be needed.

Steps taken at stage S2.1 can be summarized as follows:

S2.1.1 - Compute a so-called reference cost value J'_{ref} by minimizing

$$J'(\mathbf{a}) = W_n \sum_{l=1}^{L} \|\rho'_l(\mathbf{a})\|^2, \tag{12}$$

where $\rho'_l(\mathbf{a}) = \mathbf{e}^d_l - \mathbf{G}_{12} D(\mathbf{Ba})\mathbf{e}_l$.

S2.1.2 - Iterate the following steps:

- replace the ith $(i = 1, ..., N_a)$ B-spline (at scale n, if $n > 0$) by its finer-scale B-splines (i.e., basis at scale $n - 1$),
- from equation (12), compute the corresponding cost value J'_i,
- put back the ith B-spline.

S2.1.3 - Replace the B-splines in $\mathbf{B}$ by their finer-scale counterparts only if this influences the reconstruction in 'good' fashion, i.e., if the cost values calculated above satisfy the following criterion:

$$\frac{J'_{ref} - J'_i}{\max_{i=1,...,N_a}(J'_{ref} - J'_i)} > Th \tag{13}$$

where Th is a threshold to be fixed. The choice of Th (which can be from 0 to 1), due to our experiment, is easy to do since it has a 'large' validity band. In the presented results (section 4), Th was fixed, in general, to 0.7.

In stage S2, one also considers that, if it is not possible to refine a B-spline function at a given scale during three successive iterations, one keeps this function (i.e, one does not try again to refine it).

In this contribution, one chooses a refinement scheme based on a 'one-by-one' basis test and then one replaces the B-splines which meet the criterion in step S2.1.3. This can be seen as an approximation to a more general scheme where all combinations of refinements would be tested in order to determine the 'best one'. But an important

increase of computational time is expected here, due to increase of complexity, so one uses the simple procedure at this time.

Also, one considers that the criterion chosen in order to refine the spline representation (equation (13)) permits us to introduce finer-scale functions efficiently (i.e., within the objects and their neighborhoods). One does not test whether or not it is interesting to replace finer scales by coarser ones in the representation, avoiding in particular a considerable increase in computational time. Let us notice that this is in contrast with previous contribution [10].

Finally, the estimated object is composed of functions at several scales (e.g., figure 3.c).

As already said in the introduction, the proposed adaptive multiscale approach looks somewhat like the adaptive B-spline approach proposed earlier in [2]. However, the tools used now are quite different; what matters the most now is that one aims at achieving a localized description of the search domain and so suppress the potential artifacts (due to our previous representation).

3.3. Implementation considerations

Since the electrical parameter distribution to be estimated is most probably complex-valued (the real part represents the permittivity and the imaginary part is associated with the conductivity), following [5], the contrast function is taken as

$$\chi = \xi + i\eta, \tag{14}$$

where ξ and η are two real-valued auxiliary parameters. Then, the problem is transformed into the minimization of J depending on the two auxiliary vector parameters $\mathbf{a}_\xi$ and $\mathbf{a}_\eta$ (see [2] for more details). This formulation provides an efficient representation for the real part and for the imaginary part of the contrast vector via suitable matrices $\mathbf{B}_\xi$ and $\mathbf{B}_\eta$ (i.e., the distribution of the spline functions at several scales) for both parts (see results in section 4.5).

In the two-scale relation (equation (8)) for stage S2, the expansion coefficients α_k are fixed to 1, i.e., the matrix $\mathbf{B}$ is made of 'normalized' B-splines (see figures 3.b and 3.c). In fact, this has no influence since the expansion coefficient vector $\mathbf{a}$ is also acting on each bases.

The initial guest of the algorithms (pixel-based one and adaptive multiscale one) have been fixed to zero. Of course it is possible to use a backpropagation technic to find an initial guest but, in our case, the final results have been about the same. In fact, with these algorithms, starting from zero, the first iteration is pretty much the same as a backpropagation. Moreover, for the adaptive multiscale algorithm, the initial scale of the used splines must be fixed. It is not interesting to start with an important coarse scale (i.e., one function represente the all domain research) since in the refinement step this function will be of course replace by its finer-scale representation and because in this case the initial guste of the corresponding stage S2 will give any interesting value

(i.e, it is like start again with zero as initial guess). So this will lead to do inversion step for nothing.

4. Numerical results

4.1. Model parameters

The simulated experimental system (see figure 1) consists of N_s line sources regularly spaced between -5 m and +5 m at $y_s = 0.5$ m, and of N_r sensors regularly spaced between -10 m and +10 m at $y_r = 0.125$ m. Frequency operation is $f = 300$ MHz. Half-space 1 is characterized by $\varepsilon_{r1} = 1$ and $\sigma_1 = 0$ S.m^{-1} and half-space 2 by $\varepsilon_{r2} = 2$ and $\sigma_2 = 0$ S.m^{-1}.

The results displayed in the paper consist of maps of electrical contrasts corresponding to a search domain 1×1 m^2 sized and centered at $(x = 0.0$ m, $y = -0.5$ m$)$.

In what follows, different configurations are investigated in order to appraise the proposed approach. Reconstructions obtained using a pixel-based conjugate-gradient (PB) algorithm [2] and the adaptive multiscale (AM) method are shown.

4.2. Configuration I: single object with positive contrast

The first configuration consists in a square dielectric cylinder with permittivity $\varepsilon_{r\Omega_1} = 3$ (see figure 3). This object is 0.22 m sized and centered at $(x = 0.25$ m, $y = -0.35$ m$)$. The search domain is discretized into 33×33 cells. For this configuration, the number of receivers and sources is $N_r = 47$ and $N_s = 15$, respectively.

This simple one-object configuration is considered in order to exemplify the final distribution of the spline functions at several scales. For this configuration, the number of iterations for the minimization in step S1 is fixed to 5 and to 10 in step S2.2. The number of stage S2 is fixed to 10. Here, the global procedure is stopped after 6 stage S2 because the representation cannot be refined anymore (i.e, it is not 'interesting', due to our criterion, to replace any B-spline by its finer scale representation).

Figure 3.a shows the simulated object, figure 3.b the spline distribution at the coarse scale made of 25 B-spline basis functions, figure 3.c the retrieved map of the search domain, and figure 3.d the corresponding distribution of B-splines made of 275 functions at several scales, to be compared with the 1089 pixels of the discretized search domain.

Figure 5 gives an idea of the evolution of the global number of B-spline functions and of the number of B-splines for each scale at each iteration of the global procedure: the number of functions at stage S1 correspond to iteration 0 and the number of functions at each stage S2 corresponds to iterations i $(i > 0)$. Figure 6 gives the behaviour of the cost functional during the iterative procedure.

One can also notice that the computational time is increase (here about 30%) with the AM method due to the refinement procedure. A future work would be on the improvement of this particularly important stage.

As last remark about the algorithm and this configuration, one has considered in step S2.1 that the internal field is supposed unchanged. Figure 4 show the results obtained within this consideration (same as figure 3.c) and when the internal field is updated during this step. These results are very closed even if it seems that the reconstruction obtain by updating the internal field is a little less of good quality (perhaps due to a less appropriate parameter or criterion). The final number of spline functions in this last case is 255. Moreover, in this case, the computational time is, of course, strongly increased. So from this results, and other obtained reconstructions, the considered 'linearization' in step S2.2 is appropriated and justified.

4.3. Configuration II: two objects with positive contrasts

The second configuration is made of two dielectric cylinders (see figure 7). The lower one is square-sized with side 0.25 m, centered at ($x = 0.2$ m, $y = -0.8$ m), and with permittivity $\varepsilon_{r\Omega_1} = 3$. The upper one is rectangular with sides 0.2 m (along x) and 0.25 m (along y), centered at ($x = -0.25$ m, $y = -0.25$ m), and with permittivity $\varepsilon_{r\Omega_2} = 4$. The search domain is discretized into 33×33 cells. For this configuration, the number of receivers and sources is $N_r = 47$ and $N_s = 15$, respectively.

The simulated configuration and the results obtained using a PB method and the AM approach are shown in figure 7. In this case, starting from the same coarse scale representation as for configuration I, the final estimate obtained with the AM approach is enhanced in comparison with the one yielded by the PB method (see the Peak Signal to Noise Ratio – $PSNR$ – results in the next part). Table 1 gives the values of several parameters. The number of iterations in both inversion algorithms is specified first. For the AM approach one gives the number of iterations in stage S1, the number of stages S2, and the number of iterations in step S2.2 in the following way (S1+S2×S2.2). Note that the indicated number of iterations in stage S2 corresponds to the number of iterations reached when the procedure is stopped (i.e, here, it is not possible to refine anymore the representation). In the Table, one specifies also the maximum value of the permittivity of the reconstructed objects and the number of elements to be estimated (1681 pixels for the PB approach, 260 multiscale B-splines reached at the end of the AM procedure).

4.3.1. Noise effect In order to show the influence of noise on the reconstructions, the previous configuration is considered with noise added to the scattered field as follows:

$$\mathbf{e}_b^d = \mathbf{e}^d(1 + r\exp(i\phi)), \qquad (15)$$

where r is the percentage of added noise and ϕ is a vector of random numbers in the range $[0, 2\pi]$.

To compare the reconstructions, depending on the noise level, the Peak Signal to Noise Ratio ($PSNR$), which is commonly used in image processing, is introduced. It is

defined for a b bits gray level by:

$$PSNR = 10 \log \left(\frac{(2^b - 1)^2}{d} \right),$$ (16)

where d is the mean quadratic error given for a $[N_x \times N_y]$ image by:

$$d = \frac{1}{N_x N_y} \sum_{i=0}^{N_x - 1} \sum_{j=0}^{N_y - 1} (I_0(i, j) - I_1(i, j))^2,$$ (17)

where I_0 is the true image (simulated object) and I_1 is the reconstructed image.

Figure 8 shows the evolution of the $PSNR$ for the adaptive multiscale approach (black line) and the pixel-based approach (dashed line) for various noise levels and figure 9 shows the reconstructions obtained for the scattered field with a noise level $r = 40\%$. From these results one can observe that addition of noise strongly affects the quality of the reconstructions (the $PSNR$ decreases with the increase of added noise) obtained with the PB method. This effect is smaller with the proposed AM scheme. Hence, by controlling the degree of freedom of the inversion procedure one obtains a degree of robustness that does not require the use of an explicit regularization functional. As indicated in the introduction, at coarse scales, this spline representation enforces smoothness conditions.

4.3.2. Limited data In this part, our approach is tested against limited data, i.e. the number of receivers and sources is $N_r = 15$ and $N_s = 5$, respectively. As it is a more challenging problem, due to the small number of available data, the number of iterations in stage S2.2 has been increased.

The results are shown in figure 10. The AM approach leads to an enhancement of the final estimates of the objects. Table 2 gives, like in Table 1, the values of parameters of interest. In addition, one specifies the $PSNR$-value which 'quantifies' the quality of the AM reconstruction in comparison with the PB reconstruction. In this case both reconstructions are very closed. The deeper object is perhaps a little better reconstructed with the AM algorithm.

4.4. Configuration III: two objects with positive or negative contrasts

In this configuration, there are two dielectric cylinders with permittivity $\varepsilon_{r\Omega_1} = 1$ and $\varepsilon_{r\Omega_2} = 4$ (see figure 11). The shallower one (Ω_2) is rectangular with sides 0.2 m (along x) and 0.25 m (along y) and centered at ($x = -0.25$ m, $y = -0.25$ m). The deeper one (Ω_1) is square-sized with side 0.25 m and is centered at ($x = 0.2$ m, $y = -0.8$ m). The search domain is discretized into 33×33 cells. For this configuration, the number of receivers and sources is $N_r = 47$ and $N_s = 15$, respectively.

Figure 11 shows the simulated configuration and the reconstructions obtained with the PB method and the AM approach. One can notice an enhancement of the solution using the AM method. Table 3 shows the different parameter values. Starting from a distribution of 25 basis functions, the final distribution is made of 207 basis functions (at

several scales). Again, this should be compared with the 1089 elements to be estimated in the pixel-based approach.

4.5. Configuration IV: two objects, one conductive, one dielectric

This configuration consists in two cylinders: a dielectric one with permittivity $\varepsilon_{r\Omega} = 3$ and a metallic one with conductivity $\sigma_\Omega = 1$ S.m^{-1} (see figures 12.a and 12.d). The dielectric object is square-sized with sides 0.17 m and centered at ($x = -0.25$ m, $y = -0.32$ m). The metallic one is rectangular with sides 0.35 m (along x) and 0.25 m (along y) and centered at ($x = 0.2$ m, $y = -0.75$ m). The search domain is discretized into 41×41 cells. For this configuration, the number of receivers and sources is $N_r = 47$ and $N_s = 15$, respectively.

Figure 12 shows the obtained results for this challenging problem and Table 4 gives the parameter values. Overall, though the results are not very good, and real and imaginary parts tend to get mixed together, one can notice that the two objects can be detected with the AM scheme and not with the PB one. Moreover, for the PB method, the value of σ in Table 4, has no meaning since in effect the conductive object is not detected.

5. Conclusion

In this contribution an adaptive multiscale scheme based on the use of spline pyramids has been investigated. This coarse-to-fine based procedure takes advantage of the smoothness conditions imposed by the spline representation, which tends to regularize the problem. It is an adaptive multiscale scheme since one automatically introduces finer-scale representations within interesting areas (i.e., near and within objects in the search domain) so that the final estimate is made of spline functions at several scales. The proposed approach leads to a reduction of the number of unknows in the problem, improves the robustness of the inversion procedure, and enhances the final localization and characterization of buried objects. This enhancement is particularly notable for challenging problems like with the noised data and with the two metallic and dielectric objects.

A number of algorithmic issues remain even in this rather ideal 2-D scalar case. In particular, it would be useful to develop a clever (and computationally cheap) method to replace fine-scale B-splines by coarse-scale ones if that appears needed. As for the testing of several simultaneous changes in different locations, it is at this time an open issue.

References

[1] A. Baussard and E.L. Miller, *Detection and characterization of buried objects using an adaptive B-spline scheme*, 2003 IEEE Conference on Geoscience and Remote Sensing (IGARSS), Toulouse, vol. 6, pp. 3833-3835, July 2003.

[2] A. Baussard, E.L. Miller, and D. Prémel, "Adaptive B-spline scheme for solving an inverse scattering problem," *Inverse Problems*, vol. 20, no. 2, pp. 347-365, 2004

[3] W.C. Chew, and Y.M. Wang, "Reconstruction of two-dimensional permittivity distribution using the distorted born iterative method," *IEEE Trans. Medical Imaging*, vol. 9, no. 2, pp. 218-225, 1990.

[4] P. Dierckx, *Curve and Surface Fitting with Splines.* New York: Oxford University Press, 1993.

[5] C. Dourthe, C. Pichot, J.Y. Dauvignac, L. Blanc-Féraud, and M. Barlaud, "Regularized bi-conjugate gradient algorithm for tomographic reconstruction of buried objects," Special issue on problems on random scattering and electromagnetic wave sensing, *IEICE Trans. Electronics*, vol. E83-C, no. 12, pp. 1858-1863, 2000.

[6] B. Duchêne, and W. Tabbara, "Characterization of a buried cylindrical object from its scattered field," *IEEE Trans. Sonics Ultras.*, vol. 31, pp. 658-663, 1984.

[7] F.R. Harrington, *Field Computation by Moment Methods.* Macmillan (New York), 1968.

[8] N. Joachimowicz, C. Pichot, and J.P. Hugonin, "Inverse scattering: an iterative numerical method for electromagnetic imaging," *IEEE Trans. Antennas Propagat.*, vol. 39, pp. 1742-1751, 1991.

[9] R.E. Kleinman and P.M. Van den Berg, "A modified gradient method for two dimensional problems in tomography," *J. Comput. Appl. Math.*, vol. 42, pp. 17-35, 1992.

[10] E.L. Miller, I. Yavuz, L. Nicolaides, and A. Mandelis, "An adaptive multiscale inverse scattering approach to photothermal depth profilometry," *Circuits, Systems, and Signal Processing*, special issue on advanced signal/image reconstruction, vol. 19, no. 4, pp. 339-363, 2000.

[11] G. Strang and T. Nguyen, *Wavelet and Filter Banks*, Wellesley-Cambridge Press, Wellesley, MA, 1996.

[12] P. Thévenaz, U.E. Rittimann, and M. Unser, "A pyramidal approach to subpixel registration based on intensity," *IEEE Trans. Image Processing*, vol. 7, no. 1, pp. 27-41, 1998.

[13] M. Unser, "Splines: a perfect fit for signal and image processing," *IEEE Signal Processing Mag.*, vol. 16, no. 6, pp. 22-38, 1999.

[14] P.M. Van den Berg and R.E. Kleinman, "A contrast source inversion method," *Inverse Problems*, vol. 13, pp. 1607-1620, 1997.
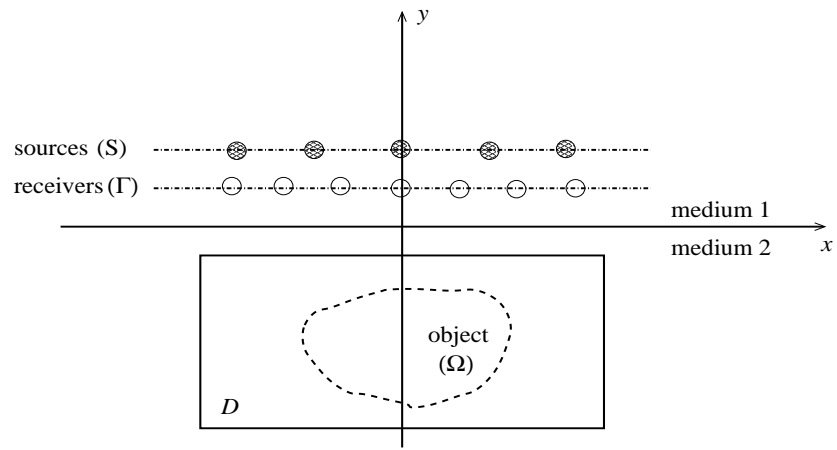
Figure 1. Geometrical configuration of study

(a)   (b)
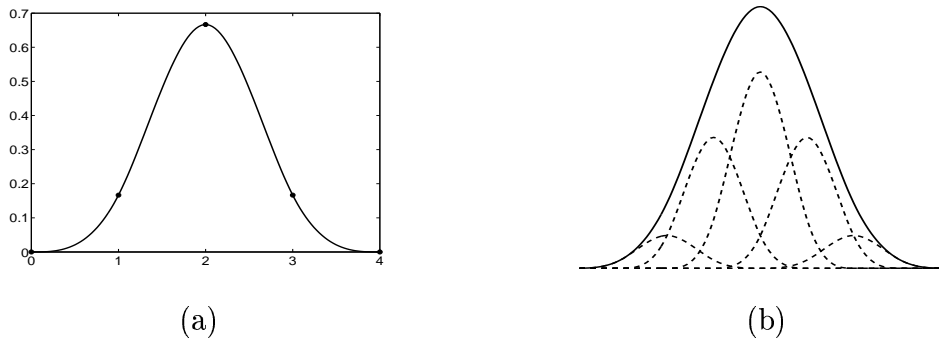
Figure 2. (a) one-dimensional cubic B-spline (scale 0, i.e, finer scale). (b) two-scale relation for the cubic B-spline: scale n (-) and scale $n-1$ (- -).
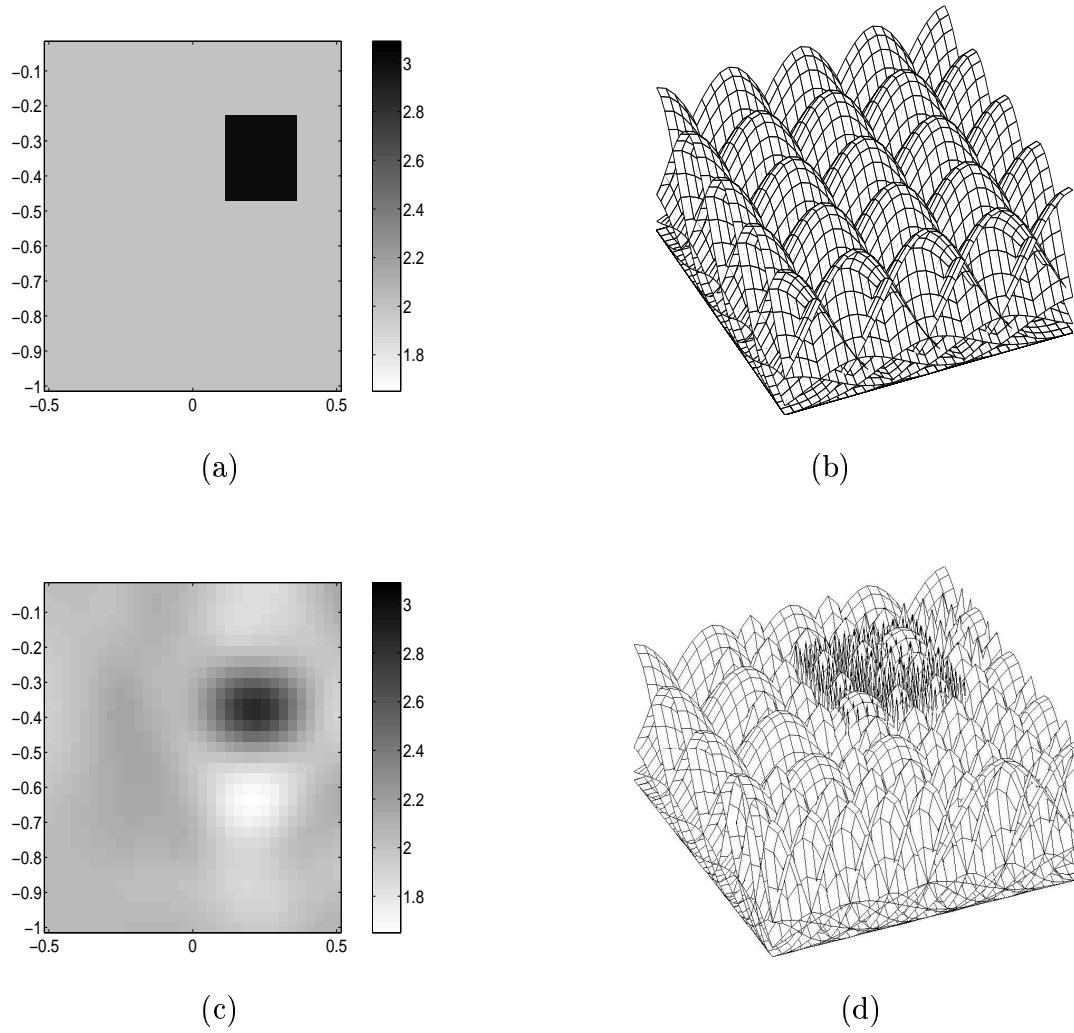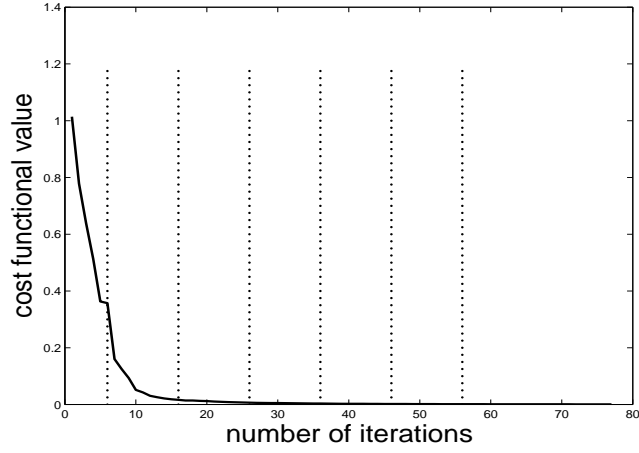
Figure 3. (a) simulated configuration. (b) initial coarse-scale made of 25 B-splines (at scale 3). (c) reconstruction reached by the adaptive multiscale method. (d) final distribution made of 275 B-splines at several scales (scales: 3, 2, 1, 0).

(a)   (b)   (c)
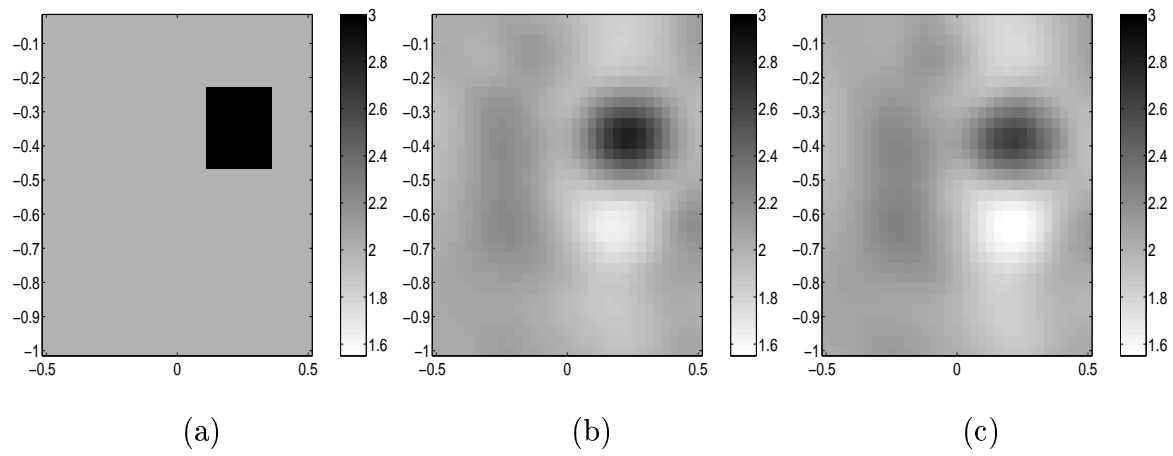
Figure 4. (a) simulated configuration. Reconstruction obtained using the adaptive multiscale method considering the total field (b) unchanged and (c) updated in step S2.2.
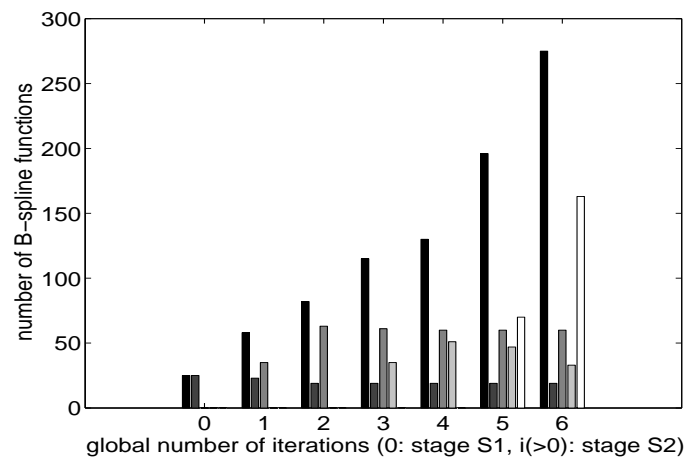
Figure 5. Evolution of the number of B-spline functions. For each iteration, from left to right: global number of B-spline functions, number of functions at scale 3, 2, 1, and 0.

Figure 6. Evolution the cost functional value (equation (10)) during the process. The vertical dashed-lines highlight the begining of a new stage S2.

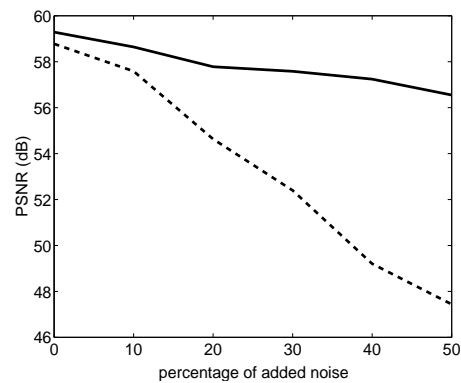   (a)   (b)   (c)
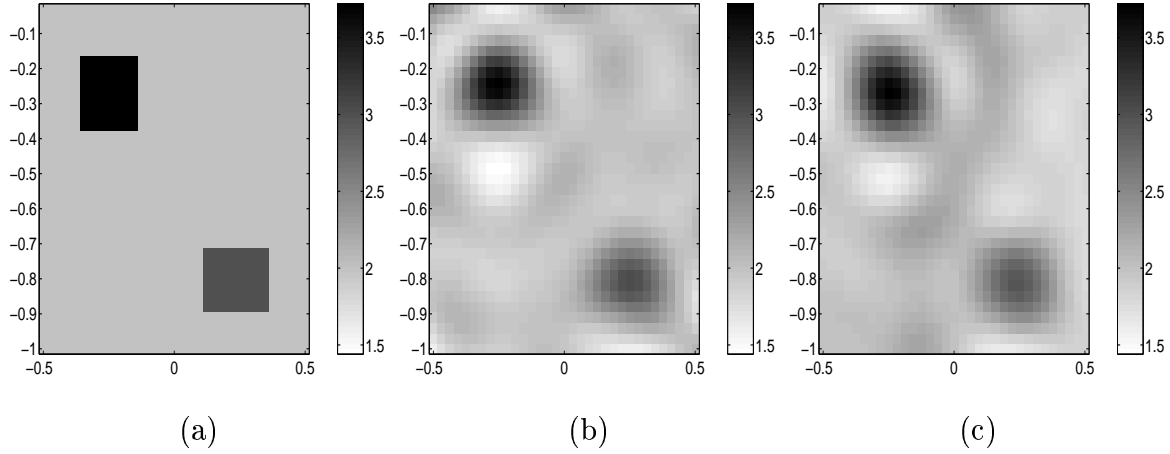
Figure 7. (a) simulated configuration. Reconstruction obtained using (b) the pixel-based method and (c) the adaptive multiscale approach.

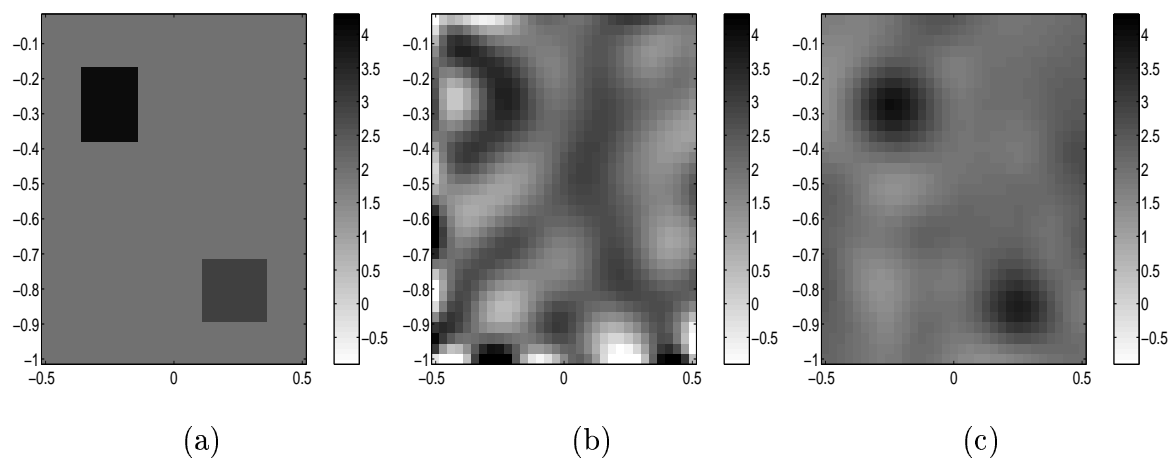**Table 1.** Values of several parameters for configuration II.

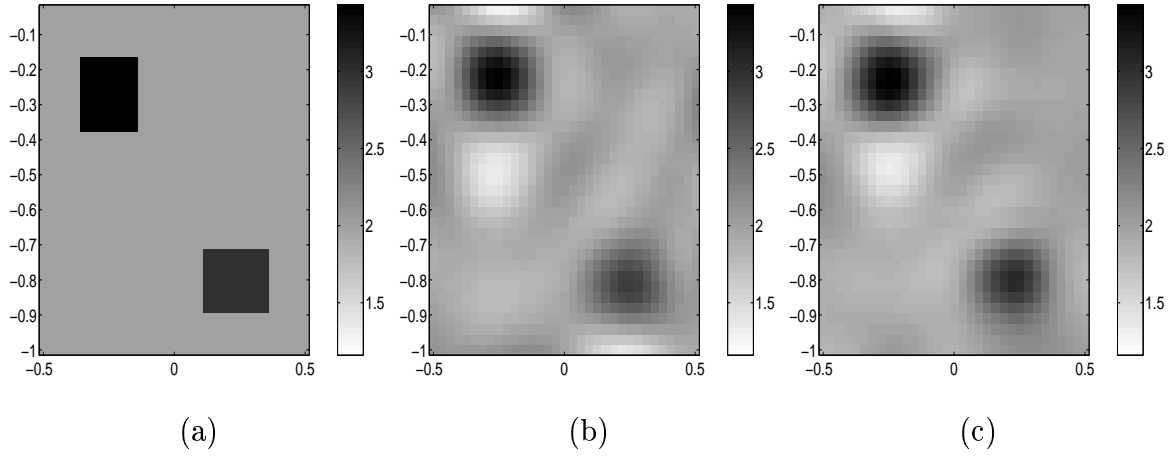|	simulated object	PB method	AM approach
iterations		65	$5 + 6 \times 10$
$\varepsilon_{r\Omega_1}$	3	3.02	2.99
$\varepsilon_{r\Omega_2}$	4	3.72	3.77
number of elements	1089	1089	260

Figure 8. Peak Signal to Noise Ratio ($PSNR$) evolution for (- -) the pixel-based method and for (-) the adaptive multiscale approach, depending on the added percentage of noise.

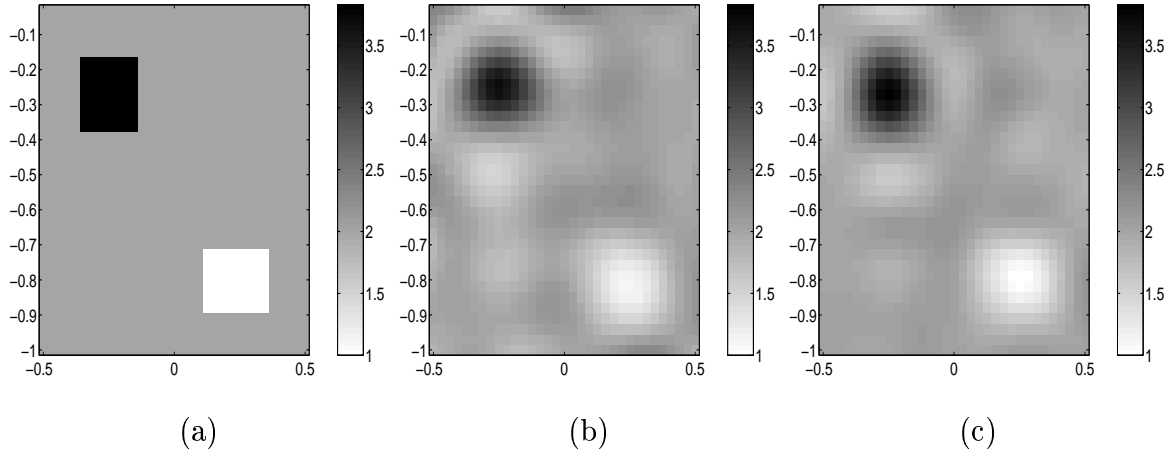(a)   (b)   (c)

Figure 9. (a) simulated configuration. Reconstruction obtained using (b) the pixel-based algorithm and (c) the adaptive multiscale method from the 40% noised data.

Figure 10. (a) simulated configuration. Reconstruction obtained using (b) the pixel-based algorithm and (c) the adaptive multiscale method.

**Table 2.** Parameter values for the configuration II with the limited data.

	simulated object	PB method	AM approach
iterations		95	$5 + 6 \times 15$
$\varepsilon_{r\Omega_1}$	3	2.89	3.07
$\varepsilon_{r\Omega_2}$	4	3.43	3.48
number of elements	1089	1089	198
$PSNR$ (dB)		57.38	57.62

(a)　　　　　　　　(b)　　　　　　　　(c)

Figure 11. (a) simulated configuration. Reconstruction obtained using (b) the pixel-based algorithm and (c) the adaptive multiscale method.

Table 3. Same as Table 2 for the configuration III.

	simulated object	PB method	AM approach
iterations		65	$5 + 6 \times 10$
$\varepsilon_{r\Omega_1}$	1	1.10	0.99
$\varepsilon_{r\Omega_2}$	4	3.67	3.83
number of elements	1089	1089	207
$PSNR$ (dB)		58.78	59.98
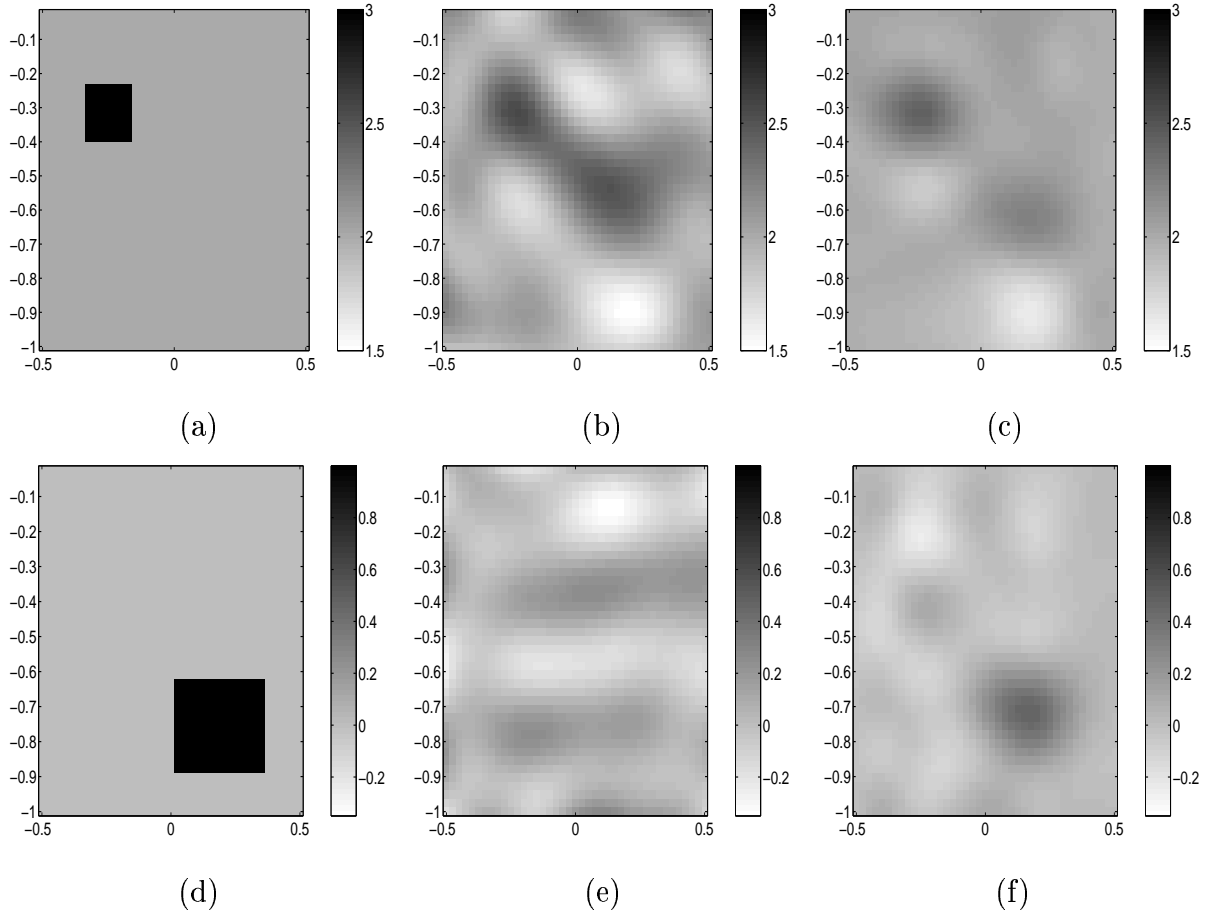
Figure 12. (a) real and (d) imaginary parts of the simulated configuration. (b) real and (e) imaginary parts of the contrast solution obtained using the pixel-based algorithm. (c) real and (f) imaginary parts of the reconstructed contrast solution obtained using the adaptive multiscale method.

Table 4. Value of several parameters for the configuration IV.

	simulated object	PB method	AM approach
iterations		65	$5 + 5 \times 12$
$\varepsilon_{r\Omega}$	3	2.56	2.43
σ_{Ω} (S.m^{-1})	1	0.27	0.47
number of elements for the real part	1681	1681	269
number of elements for the imaginary part	1681	1681	218
$PSNR$ for the real part (dB)		61.58	64.36
$PSNR$ for the imaginary part (dB)		58.44	60.57